ADVANCED MATERIALS
www.advmat.de

Universal Ion Migration Suppression Strategy Based on Supramolecular Host–Guest Interaction for High-Performance Perovskite Solar Cells

Dongmei He, Danqing Ma, Jiajia Zhang, Yingying Yang, Jike Ding, Cong Liu, Xinxing Liu, Yue Yu, Tao Liu, Cong Chen,* Meicheng Li,* and Jiangzhao Chen**

The migration of multiple chemical species is are main factor leading to the intrinsic instability of perovskite solar cells (PSCs). Herein, a universal ion migration suppression strategy is innovatively reported to stabilize multiple functional layers by simultaneously suppressing the migration of multiple mobile chemical species based on host–guest interaction via calixarene supramolecules. After incorporating 4-tert-butylcalix[8]arene (C8A), the interfacial defects are passivated, suppressing trap-assisted nonradiative recombination. Moreover, the p-doping of Spiro-OMeTAD is facilitated, and the extraction and transport of holes are promoted for n-i-p regular PSCs. The C8A doped regular devices based on the two-step perovskite deposition method achieve a power conversion efficiency (PCE) of 26.01% (certified 25.68%), which is the record PCE ever reported for the TiO_2-based planar PSCs. The C8A passivated p-i-n inverted PSCs obtain a champion PCE of 27.18% (certified 26.79%), which is the highest PCE for the PSCs using the vacuum flash evaporation method. The resulting unsealed inverted device retains 95% of its initial PCE after 1015 h of continuous operation at maximum power point. This work provides a feasible and effective avenue to address the intrinsic instability of perovskite-based photovoltaics and other optoelectronic devices.

1. Introduction

Recently, perovskite solar cells (PSCs) developed by several groups have demonstrated distinguished power conversion efficiencies (PCEs) exceeding 26%, which exhibits immense commercial application prospects.[1–3] However, the practical deployment of PSCs is still impeded by their poor long-term stability. In practice, the stability of PSCs is mainly determined by all functional layers and their interfaces. Among them, the carrier transport layer (CTL), the perovskite layer, and the metal electrode (usually Au and Ag) play a crucial role in accomplishing operably stable and efficient PSCs. The intrinsic instability induced by the above functional layers poses a severe challenge for the commercial application of perovskite photovoltaic technology.

One of the key reasons responsible for device instability is the intrinsic soft ionic nature of the perovskite layer. The A-site

D. He, X. Liu, Y. Yu, J. Chen
Faculty of Materials Science and Engineering
Kunming University of Science and Technology
Kunming 650093, China
E-mail: jzchen@kust.edu.cn

D. Ma
Key Laboratory of Optoelectronic Technology & Systems (Ministry of Education)
College of Optoelectronic Engineering
Chongqing University
Chongqing 400044, China

J. Zhang
Anhui Provincial Key Laboratory of Green Carbon Chemistry
College of Chemistry and Materials Engineering
Fuyang Normal University
Fuyang 236037, China

The ORCID identification number(s) for the author(s) of this article can be found under https://doi.org/10.1002/adma.202505115

DOI: 10.1002/adma.202505115

Y. Yang, M. Li
State Key Laboratory of Alternate Electrical Power System with Renewable Energy Sources
School of New Energy
North China Electric Power University
Beijing 102206, China
E-mail: mcli@ncepu.edu.cn

J. Ding, C. Chen
State Key Laboratory of Reliability and Intelligence of Electrical Equipment
School of Materials Science and Engineering
Hebei University of Technology
Tianjin 300401, China
E-mail: chencong@hebut.edu.cn

C. Liu, T. Liu
State Key Laboratory of Featured Metal Materials and Life-cycle Safety for Composite Structures
School of Resources
Environments and Materials
Guangxi University
Nanning 530004, China
E-mail: liutaozhx@gxu.edu.cn

organic cations in octahedron of perovskite, like formamidinium (FA^+) and methylammonium (MA^+), easily evaporate under thermal stress, and the X-site halide ions (like I^- and Br^-) are prone to migrate to CTL and the interface between CTL and metal electrode, resulting in lattice distortion of halide perovskite.[4,5] The chemical interaction between positive radicals of CTL and the invasive I^- can lead to the rapid attenuation of hole conductivity and a more incompatible band alignment. In addition, the abundant defects ineluctably exist at the grain boundaries (GBs) surface of perovskite films during the crystallization process of perovskite.[6] These defects could not only capture free charge carriers and then result in serious trap-assisted nonradiative recombination losses, but also accelerate the migration of organic cations and halide anions under external stimuli such as light and thermal stress, leading to the decomposition of perovskite and irreversible damage to other functional layers.[7,8] As such, inhibiting the migration of FA^+ and I^- ions, suppressing volatilization of organic cations, and passivation of defects are crucial for improving the stability of the perovskite layer and device.

Besides, the terrible operational instability issues of PSCs are not only caused by the intrinsic properties of the perovskite layer, but also by those of the metal electrode. Lee et al. found that the corrosion of metal electrodes is one of the major origins of intrinsic device degradation during the self-degradation process of PSCs.[9] In effect, the silver electrode is prone to diffuse into other functional layers after long-term operation of PSCs at high temperatures. The migrated I^- and diffused silver electrodes meet in various functional layers and undergo irreversible chemical reactions to generate silver iodide, leading to the rapid device degradation. Moreover, the irreversible degradation of the silver electrode is often far ahead of the degradation of the perovskite layers.[10,11] In a word, the cross migration and reaction of Ag and I^- is a huge barrier to achieving operationally stable PSCs.

Furthermore, almost all high-efficiency n-i-p regular PSCs are realized through the state-of-the-art hole transport material (HTM) of 2,2′,7,7′-tetrakis(N,N-di-4-methoxyphenyl-amine)-9,9′-spirobifluorene (Spiro-OMeTAD), which usually needs to be doped by bis(trifluoromethane) sulfonimide lithium salt (Li-TFSI) to increase conductivity and hole mobility, aiming to guarantee efficient hole extraction and transport.[1,3,12–16] Nevertheless, the incorporation of Li-TFSI causes some negative effects. On the one hand, the hygroscopicity of Li-TFSI significantly increases the humidity sensitivity of HTL and the final devices. On the other hand, the easily mobile Li^+ within the entire device due to its small size would lead to awful intrinsic stability of PSCs. Although long-term stability is remarkably enhanced by dopant-free HTM and alternative dopant strategies, these strategies show far less universal and much lower PCEs than classical Li-TFSI doping strategy.[17–21] To simultaneously obtain high PCE and excellent stability, therefore, exploring a new and effective co-dopant should be highly desirable by facilitating p-doping and inhibiting Li^+ movement.[16]

In the past decade, a lot of research has been conducted to overcome the above intractable problems, and conspicuous advancements have been obtained.[16,22–25] However, the current methods and strategies are difficult to simultaneously address different types of ion migration in multiple functional layers due to the fact that almost every functional layer in the device has ion migration issues and involves multiple types of ions or chemical compositions. In view of the complexity and urgency of the above issues, it is still an enormous challenge to develop a simple and effective approach to synchronously address them. It should be feasible to simultaneously manipulate the CTL, perovskite layer, and silver electrode by introducing a multifunctional material between the perovskite layer and silver electrode. Such a versatile molecule should be capable of forming a coordination bond with Li^+ and Ag, forming a hydrogen bond with FA^+ or I^-. Furthermore, it should possess as many active sites as possible since a multisite molecular modulator can strengthen interaction with the functional layer and thereby reach maximum potential.[26–28] After all consideration, the supermolecule should be an ideal candidate to achieve the above goal by host–guest chemistry reaction. The present studies mainly concentrated on crown ether[23,29,30] and cyclodextrin,[31,32] whereas the work on calixarene is rarely reported. It should be pointed out that crown ether and cyclodextrin are hygroscopic and can dissolve in water, while calixarene exhibits excellent moisture resistance due to multiple hydrophobic benzene rings. The function of the presently reported strategies based on host–guest chemical interactions is relatively simple, such as suppressing Li^+ migration,[23] passivate undercoordinated Pb^{2+} defects,[29,30] modulating perovskite crystallization[33] or stabilizing perovskite precursor solution.[34] Therefore, the functionality and potential of the host–guest interaction strategy should be further explored.

In this work, we for the first time proposed a multifunctional universal ion migration suppression strategy based on host–guest interaction by using calixarene supramolecules, which synchronously suppressed the migration of FA^+, I^-, Li^+, and Ag via coordination bond and hydrogen bond, enabling the successful fabrication of high-performance PSCs. A series of calixarene supramolecules with different hydroxyl number and cavity sizes, including 4-tert-Butylcalix[4]arene (abbreviated as C4A), 4-tert-Butylcalix[6]arene (abbreviated as C6A), and 4-tert-Butylcalix[8]arene (abbreviated as C8A), were used to modify perovskite layer and CTL, as well as the interface between them. On the basis of overall consideration, it was revealed theoretically and experimentally that C8A is superior to C6A and C4A. It was demonstrated that the C8A modification is universal for both n-i-p regular and p-i-n inverted PSCs. The C8A modified n-i-p regular devices based on one-step and two-step deposition methods yielded a PCE of 25.30% (certified 24.69%) and 26.01% (certified 25.68%), respectively, which is the highest certified efficiency reported for the TiO_2-based planar PSCs. The C8A modified p-i-n inverted PSCs exhibited a seductive PCE of 27.18% (certified 26.79%). Moreover, the resulting unencapsulated inverted device demonstrated excellent operational stability by maintaining 95% of its initial efficiency after 1015 h of continuous maximum power point (MPP) tracking. This work provides a meaningful thought for addressing the intrinsic instability of PSCs by using a simple and effective molecular capsule strategy based on host–guest chemistry with calixarene supramolecules.

2. Results and Discussion

2.1. Investigation on the Interaction Between Calixarenes and Multiple Mobile Chemical Species

Calix[n]arenes are [1_n]-metacyclophanes composed of phenol units bridged by methylene, which have the cone (cup) conformer. Due to its unique rigid cup-shaped structure and abundant coordination sites, calixarene supramolecules can complex ions and neutral molecules to form host–guest complexes,[35,36] which is expected to synchronously solve the migration problems of FA^+, I^-, Li^+, and Ag. In response to this, to simultaneously modulate three different functional layers involving HTL, perovskite layer, and silver electrode, 4-tert-Butylphenol (4TBP), C4A, C6A, and C8A were directly added into Spiro-OMeTAD HTL. 4TBP is the monomer used for synthesizing these calixarene supramolecules, which were used as reference molecules to study the interaction of calixarene molecules with different functional layers. As shown in Figure S1 (Supporting Information), the electrostatic potential (ESP) shows that electrons mainly distribute on —OH groups, and C8A has the highest electron density due to the presence of more —OH groups. The larger the cavity size is, the more the number of —OH in calixarene is. Therefore, the cavity size of calixarene should have a significant influence on its chemical activity. Since it is so, we first explored the interaction strength of 4TBP, C4A, C6A, and C8A with different mobile chemical species through density functional theory (DFT) calculation. Firstly, we theoretically examined the interactions between the four considered aromatic molecules and Li^+ through DFT calculations. **Figure 1a** exhibits the optimized structures of these Li^+-embedded aromatic molecules. Clearly, atoms or groups within the aromatic molecules do not reside on a plane, indicating that local structural distortions are energetically preferred. Furthermore, we observed that the number of embedded Li^+ increases with the size of the aromatic molecules. The results show that the larger the cavity size of calixarene is, the more Li^+ it can accommodate. The binding energy is increased in the order of 4TBP, C4A, C6A, and C8A. Particularly, an eight-cups C8A molecule can attract four Li^+ with an average binding energy of 1.43 eV. Experimentally, we found that the C8A solution exhibited weak acidity, suggesting the ionization of a portion of the C8A molecules. Thus, we investigated the interaction between the deprotonated C8A molecule and Li^+. It was revealed that the deprotonated C8A molecule attracts five Li^+, and the average binding energy is increased to 2.143 eV. Given that among these aromatic molecules, the C8A possesses the highest Li^+ intercalation capacity, it should be the most effective in mitigating Li^+ migration.

Since calixarene molecules were directly incorporated into HTL, they should be able to contact and interact with the Ag electrode. Consequently, it is highly imperative to gain insights into the interaction of these calixarene molecules with Ag and then understand whether they can suppress the migration of Ag atoms. Figure 1b illustrates the structures of Ag-embedded aromatic molecules. It was seen that each aromatic molecule can capture only one or two Ag atoms, with relatively low binding energies. Surprisingly, the deprotonated C8A molecule can firmly capture one Ag atom, as evidenced by the highest binding energy of 0.646 eV. Consequently, we anticipate that the C8A molecules, due to their ionization, could more effectively impede Ag migration than other smaller-sized calixarene molecules.

Similar to the Ag electrode, the calixarene molecules also would contact and interact with the surface of the underlying perovskite films. It was speculated that —OH on calixarene could passivate the undercoordinated Pb^{2+} and/or iodide vacancy defects via coordination bond and electrostatic interaction. In addition, —OH should be able to form a hydrogen bond with FA^+ and I^- within octahedra $[PbI_6]^{4-}$, which thereby holds back the volatilization of FA^+ under thermal stress and inhibits the migration of FA^+ and I^-. Given this, the interaction of doping molecules with perovskite was explored and compared. Figure 1c suggests that the binding energy of 4TBP, C4A, C6A, and C8A with the perovskite surface is 0.504, 1.449, 1.742, and 2.114 eV, respectively. Obviously, C8A exhibits the highest binding energy with the perovskite surface among all doping molecules. This indicates that C8A should be the best in passivating surface defects and suppressing the migration of FA^+ and I^-.

In a word, the larger the size of molecules is, the stronger their interaction with different functional layers is, which is due to more —OH on large calixarene molecules and a larger cavity structure. In our previous studies, it was testified that multisite molecules could have stronger interaction with functional layers and accordingly showed better device performance as compared with a single active site molecule.[37] Then, we verified the interaction of C8A with multiple mobile chemical species through experimental evidence. As presented in Figure 1d,e, after the formation of a coordination bond between Li^+ and O, the electron cloud on the oxygen atom partially transfers to the empty orbitals of Li^+, resulting in an enhanced shielding effect of Li^+ and a chemical shift toward higher field directions. Meanwhile, the shielding of adjacent hydrogen atoms is reduced after the chemical interaction between Li^+ and O, resulting in the δ signal moving toward the low field direction. It shows that —OH on C8A and Li^+ had a strong interaction. X-ray photoelectron spectra (XPS; Figure S2, Supporting Information) and Fourier transform infrared (FTIR; Figure S3, Supporting Information) spectra also confirmed the chemical interaction between —OH on C8A and Li^+. As revealed in Figure 1f, a part of the silver electrode is chemically corroded by halide ions (I^-/Br^-), transforming elemental silver (Ag^0) to Ag^+. Compared with bare Ag without C8A, the Ag with C8A exhibited much reduced Ag^+ content (Figure 1g). This is because the hydroxyl group on C8A deprotonates and interacts with Ag^0 through coordination bonds, inhibiting the migration of the silver electrode and significantly suppressing the chemical reaction between halogen ions and the electrode. Two new absorption peaks appeared near 985 and 1060 cm^{-1} in the FTIR curve of the Ag electrode modified with C8A (Figure S4, Supporting Information), belonging to the —C—O bending vibration peak and the stretching vibration peak. Moreover, the two peaks show a significant shift compared to that of pure C8A, indicating once again the host–guest chemical interaction between C8A and Ag^0. From Figure S5 (Supporting Information), the shift of the N 1s peak of the perovskite film toward higher binding energy affirmed the hydrogen bond interaction between —OH on C8A and FA^+. Besides, the rich hydroxyl groups make C8A interact with I^- through hydrogen bonding (Figure S6, Supporting Information). Moreover, FTIR spectra (Figure S7, Supporting Information) show a significant shift in the characteristic peak of

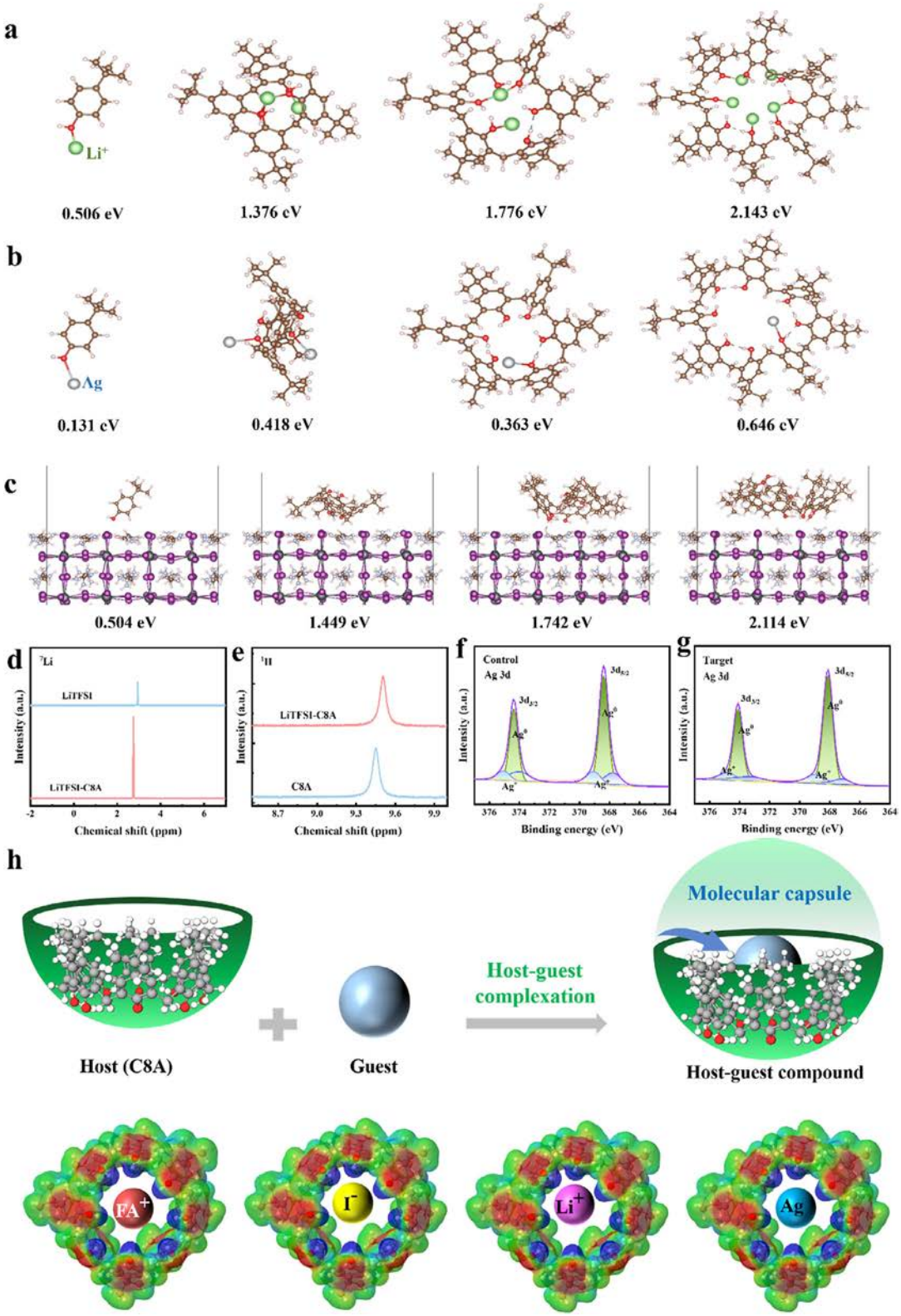

Figure 1. Theoretical and experimental investigation on the interaction between calixarenes and different functional layers. a) Binding energy of 4TBP, C4A, C6A and C8A with Li^+. b) Binding energy of 4TBP, C4A, C6A and C8A with Ag. c) Binding energy of 4TBP, C4A, C6A and C8A with perovskite. d) ^7Li NMR of the Li-TFSI solutions without and with C8A. e) ^1H NMR of the C8A solutions without and with Li-TFSI. f,g) XPS spectra of Ag 3d from Ag electrode films with and without C8A. h) Schematic diagram of ion migration suppression strategy based on host–guest interaction between C8A and multiple mobile chemical species.

—OH, indicating that C8A may interact with FA^+ and I^- through hydrogen bonding, which is consistent with the results of DFT and XPS.

In summary, as shown in Figure 1h, C8A as host can be used as a molecular capsule to encapsulate FA^+, I^-, Li^+, and Ag, serving as guests, which form stable host–guest complexes through hydrogen bonding, coordination bonding, van der Waals forces, and other interactions. The theoretical and experimental results suggest that C8A molecules should be capable of simultaneously suppressing the migration of multiple chemical species (FA^+, I^-, Li^+, and Ag) from different functional layers by a molecular capsule strategy based on host–guest interaction.

2.2. Simultaneous Suppression of Multiple Chemical Species Migration

In order to study the intrinsic stability induced by the migration of chemical species, we carried out the time-of-flight secondary ion mass spectroscopy (TOF-SIMS) and scanning electron microscope (SEM) measurements for the control and C8A modified samples after aging for 10 days under one sun illumination and at 85 °C in a nitrogen-filled glovebox. TOF-SIMS was employed to investigate the spatial distribution variation of FA^+, I^-, Li^+, and Ag in the control and C8A modified devices (both n-i-p and p-i-n) after aging under one sun illumination and at 85 °C for 10 days in a nitrogen-filled glovebox (**Figure** 2a,b). For the n-i-p device, we could observe much more Li^+ in the perovskite layer and silver electrode layer for the control device compared with the C8A doped device, indicating that C8A can inhibit the migration of Li^+ via the coordination bond between —OH and Li^+. For both n-i-p and p-i-n devices, a large amount of Ag diffused to the HTL and perovskite layer in the control device, whereas Ag was almost completely immobilized in the modified device. This implies that the migration of Ag was effectively restrained by host–guest interaction between C8A and Ag. After 10 days of aging, FA^+ had diffused to the metal electrode in the control device while FA^+ was thoroughly retained in the perovskite layer in the C8A modified device, which should be ascribed to the hydrogen bond of —OH with FA^+. It was found that I^- migrated and diffused much more to the Ag electrode layer in the control device in comparison with the C8A modified device, which should be attributed to effective passivation of undercoordinated Pb^{2+} and iodide vacancy defects, and the hydrogen bond between —OH and I^-. The above results confirmed that C8A modification could simultaneously stabilize the perovskite layer and silver electrode of both n-i-p and p-i-n devices by synchronous suppression of the migration of FA^+, I^-, Li^+, and Ag via host–guest interaction between C8A and these mobile chemical species. Moreover, C8A is uniformly distributed in HTL and does not affect the dispersion of Spiro-OMeTAD (Figure S8, Supporting Information).

Additionally, SEM was used to measure cross-sectional morphology of the PSCs without and with C8A doping under one sun illumination at 85 °C for 10 days. It can be seen clearly in Figure 2c that severe collapse of the Ag electrode layer, HTL, and perovskite layer happened in the control device after aging, while the functional layers of the C8A doped device remained almost intact under the same aging conditions. This indicates that the stability of functional layers was markedly improved after C8A doping, which is put down to the synchronous immobilization of FA^+, I^-, Li^+, and Ag through host–guest interaction by C8A supramolecules. Subsequently, we measured the surface SEM images and TOF-SIMS mapping for the HTLs without and with C8A doping after aging under one sun illumination at 85 °C for 10 days. We can observe many white particles in the pristine HTL, while no while particles appeared in the C8A-doped HTL (Figure 2d). As evidenced by TOF-SIMS mapping technology (Figure 2e), these white particles were proven to be formed by the aggregation of Li^+ after migration. C8A effectively inhibited the migration and aggregation of Li^+ via the formation of the host–guest compound with Li^+, thereby improving the homogeneity and stability of HTL.

Subsequently, we used Kelvin probe force microscopy (KPFM) to characterize the potential changes on the surface of the fresh and aged HTLs without and with C8A doping. From Figure 2f,g, the surface potential of the fresh HTL film doped with C8A was much higher than that of the pristine HTL film, due to ameliorated conductivity and mobility as well as uniformity, which is beneficial for hole extraction and transport. Most of all, compared with the undoped HTL films, C8A-doped HTL films exhibited much slower potential decrease after aging for 10 days under 40%–60% RH and at 85 °C, which is mainly because of effective suppression of FA^+, I^-, Li^+ and Ag migration by the host–guest interaction between C8A and these chemical species.

2.3. Facilitated p-Doping via C8A

Since phenolic hydroxyl is a weak acid, C8A can dissociate some hydrogen ions (H^+) due to its abundant phenolic hydroxyl. This conclusion was confirmed by high-resolution mass spectrum (HR-MS; Figure S9, Supporting Information) and ^1H nuclear magnetic resonance (^1H NMR; Figure S10, Supporting Information). It was revealed that the 8 hydrogen atoms on the phenolic hydroxyl groups of C8A turned into 7 after mixing with Li-TFSI in chlorobenzene solution, indicating the release of one H^+. As can be seen from the previous discussion, C8A is more easily coordinated with Li^+ through a coordination bond after deprotonation and forming C8A-Li^+ host–guest complexes. So, the interaction between C8A and Li^+ subsequently causes Li-TFSI to continue dissociating into free Li^+ and $TFSI^-$, and the free $TFSI^-$ combines with Spiro-OMeTAD$^{\bullet+}$ to generate stable Spiro-OMeTAD$^{\bullet+}$$TFSI^-$ by replacing O_2^-, which can further promote the oxidation of Spiro-OMeTAD.

Thus, C8A can achieve p-type doping of Spiro-OMeTAD (direct doping) and promote the doping of Spiro-OMeTAD by the interaction with Li-TFSI (indirect doping). The electron spin resonance (ESR) spectra demonstrated the above conclusions (Figure S11, Supporting Information). In the pristine Spiro-OMeTAD solution, no paramagnetic peak belonging to the radicals of Spiro-OMeTAD$^{\bullet+}$ was found because of the absence of p-dopants. In contrast, Spiro-OMeTAD-C8A solution exhibited a strong paramagnetic peak, but the peak intensity was weaker than that of Spiro-OMeTAD@Li-TFSI solution, suggesting that C8A had a weaker p-type doping ability for Spiro-OMeTAD than the conventional Li-TFSI dopant. Interestingly, upon C8A was incorporation into Spiro-OMeTAD@Li-TFSI solution, the paramagnetic peak intensity was further remarkably increased, confirming the

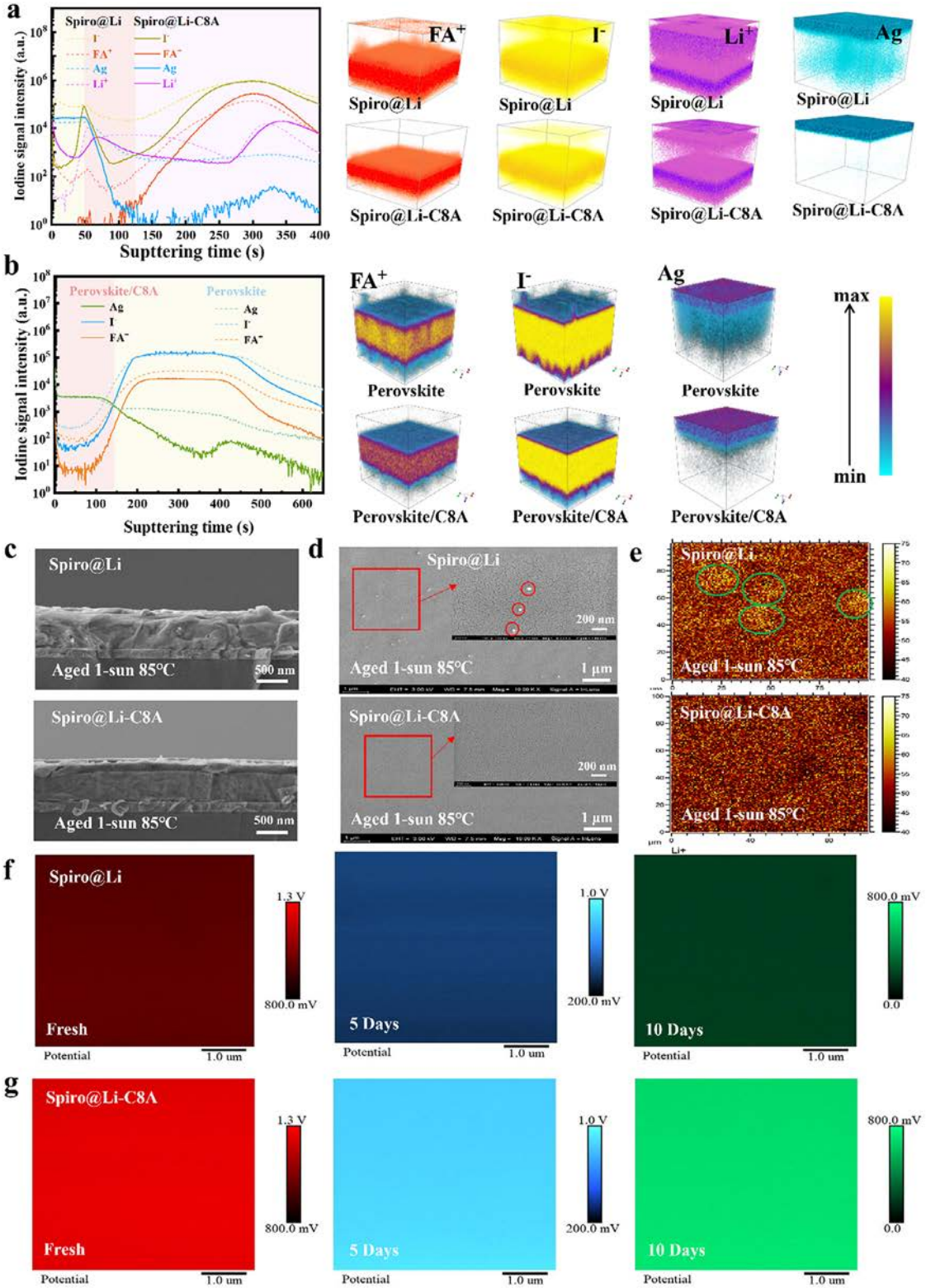

Figure 2. Simultaneous immobilization of multiple mobile chemical species from different functional layers. a) TOF-SIMS depth distribution of the complete n-i-p devices without and with C8A doping under one sun illumination at 85 °C for 10 days. b) TOF-SIMS depth distribution of the complete p-i-n devices without and with C8A modification under one sun illumination at 85 °C for 10 days. c) Cross-sectional SEM images of the PSCs without and with C8A doping under one sun illumination at 85 °C for 10 days. d) SEM images of the HTLs without and with C8A doping after aging under one sun illumination at 85 °C for 10 days. e) TOF-SIMS mapping images of the HTLs without and with C8A doping under one sun illumination at 85 °C for 10 days. f,g) KPFM of the HTLs without and with C8A doping after aging for different times under 40%–60% RH and at 85 °C.

facilitated p-doping of Spiro-OMeTAD by C8A due to the host–guest interaction between C8A and Li^+. Similarly, the UV–vis spectra also revealed the same doping tendency as ESR (Figure S11, Supporting Information). Similarly, we compared the oxidation ability of 4TBP, C4A, C6A, and C8A toward Spiro-OMeTAD using UV–vis spectra. As shown in Figure S12 (Supporting Information), C8A exhibited the best oxidation ability for Spiro-OMeTAD, which is consistent with the theoretical calculation results. In addition, the effect of C8A on the first oxidation potential of Spiro-OMeTAD was evaluated using cyclic voltammetry (CV). The Spiro-OMeTAD, Spiro-OMeTAD-C8A, Spiro-OMeTAD@Li-TFSI, and Spiro-OMeTAD@Li-TFSI-C8A versus $Ag/AgNO_3$ electrodes showed the values of 1.03, 1.08, 1.25, and 1.35 V, respectively (Figure S13, Supporting Information). The large potential difference is beneficial for the occurrence of the oxidation reaction. It can be concluded that introducing C8A into conventional doping of Li-TFSI can better oxidize Spiro-OMeTAD, which again verifies the results of ESR. Next, we verified the improvement of HTL conductivity by C8A doping. The conductivity and hole mobility were enhanced from Spiro-OMeTAD, Spiro-OMeTAD-C8A, Spiro-OMeTAD@Li-TFSI, and Spiro-OMeTAD@Li-TFSI-C8A (Figures S14 and S15, Supporting Information), which testified to the doping functions of C8A for Spiro-OMeTAD via host–guest complexation. This shows that host–guest complexation interaction between C8A and Li^+ can not only suppress the migration of Li^+ but also promote the p-doping of Spiro-OMeTAD. In addition, as depicted in the energy level arrangement diagram drawn based on UPS calculation results (Figures S16 and S17, Supporting Information), the energy offset between HOMO of the HTL film doped with C8A and the valence band maximum (VBM) of perovskite film is reduced as compared to that between HOMO of HTL without C8A doping and the VBM of perovskite film, which should be beneficial for hole extraction.[38]

2.4. Surface Defect Passivation by C8A

As the dopant for HTL, it has been proved that C8A was uniformly distributed within HTL, which inhibited the migration and aggregation of Li^+ by host–guest complexation. We have theoretically confirmed the passivation effect of C8A for the surface defects of perovskite films. To experimentally confirm the passivation effect of C8A, the defect density was calculated by the space charge limited current (SCLC) technique. Figure S18 (Supporting Information) showed significant decrease in defect density from 1.61×10^{16} cm^3 to 1.10×10^{16} cm^3 after C8A doping into HTL in regular devices, and from 1.22×10^{16} cm^3 to 9.80×10^{15} cm^3 after C8A modification in inverted devices, indicating that C8A molecules can effectively passivate surface defects of perovskite films, such as undercoordinated Pb^{2+} and iodide vacancy defects. Additionally, the C8A-modified perovskite film exhibited a stronger photoluminescence emission intensity (Figure S19a, Supporting Information) and a longer charge carrier lifetime (Figure S19b, Supporting Information), which confirmed the in situ passivation of the defects on perovskite surface by C8A and the inhibition of nonradiative charge recombination at the perovskite/HTL interface. Interestingly, the PL peak shift in spectra can once again be confirmed that C8A effectively passivates interfacial trap states.[39,40] Subsequently, the XPS spectra in Figure S20 (Supporting Information) revealed that the main types of defects passivated by C8A are undercoordinated Pb^{2+} and/or iodide vacancy defects. Hence, with the passivation of iodide vacancy defects, the migration of iodide ions was also inhibited.

2.5. Multifunctionality of C8A

As demonstrated above, C8A can interact with FA^+, I^-, Li^+, and Ag and suppress their migration, where C8A acted as a molecular capsule by incorporating these chemical species into its cavity (**Figure 3a**). FA^+, I^-, Li^+, and Ag are difficult to migrate because they were firmly immobilized and locked in the cavity of C8A calixarene supramolecules based on host–guest interaction. Through the molecular capsule strategy, the Ag electrode layer, HTL, and perovskite layer were stabilized. Besides, the defects (e.g., undercoordinated Pb^{2+} and halide vacancy defects) on the surface of perovskite films can be effectively passivated via coordination bond and hydrogen bond, thereby inhibiting trap-induced nonradiative recombination (Figure 3b). Moreover, more $TFSI^-$ would be generated after the host–guest complexation between C8A and Li^+, which can combine with Spiro-OMeTAD$^{\bullet+}$ to form stable Spiro-OMeTAD$^{\bullet+}$$TFSI^-$, accelerating the oxidation of Spiro-OMeTAD (Figure 3c). In short, C8A can play multiple functions of suppressing the migration of multiple chemical species, passivating the surface defects of perovskite films, as well as promoting the doping of Spiro-OMeTAD.

2.6. Photovoltaic Performance

As discussed above, the calixarene supramolecules with different cavity sizes exhibited different defect passivation and doping effectiveness. The effect of different calixarene doping on photovoltaic performance was investigated by fabricating regular planar PSCs based on a one-step deposition method in ambient air. The doping concentration of different calixarenes was optimized (Figures S21–S24, Supporting Information). Among all investigated doping molecules, the C8A-doped device exhibited the best photovoltaic performance with the highest values of all photovoltaic parameters (Figures S25 and S26, Supporting Information). The champion PCEs of the control, 4TBP, C4A, and C6A doped devices were 22.05%, 23.6%, 24.0%, and 24.8%, respectively (**Figure 4a**; Figure S27, Supporting Information). In comparison, the C8A doped device achieved a maximum PCE of 25.30%, with a short-circuit current density (J_{SC}) of 24.91 mA cm^{-2}, an open-circuit voltage (V_{OC}) of 1.195 V, and a fill factor (FF) of 85.0%, which is among the highest PCEs for the regular PSCs fabricated in ambient air. The integrated current density is consistent with the J_{SC} values extracted from J–V curves (Figure S28, Supporting Information). We also obtained a certified PCE of 24.69% for the devices based on a one-step deposition approach (Figure S29, Supporting Information). Compared with the control device, the C8A modified device had an increased J_{SC}, which is attributed to facilitated hole extraction and transport due to improved electric properties of HTL and reduced interfacial defects. After C8A doping, the V_{OC} and FF were improved,

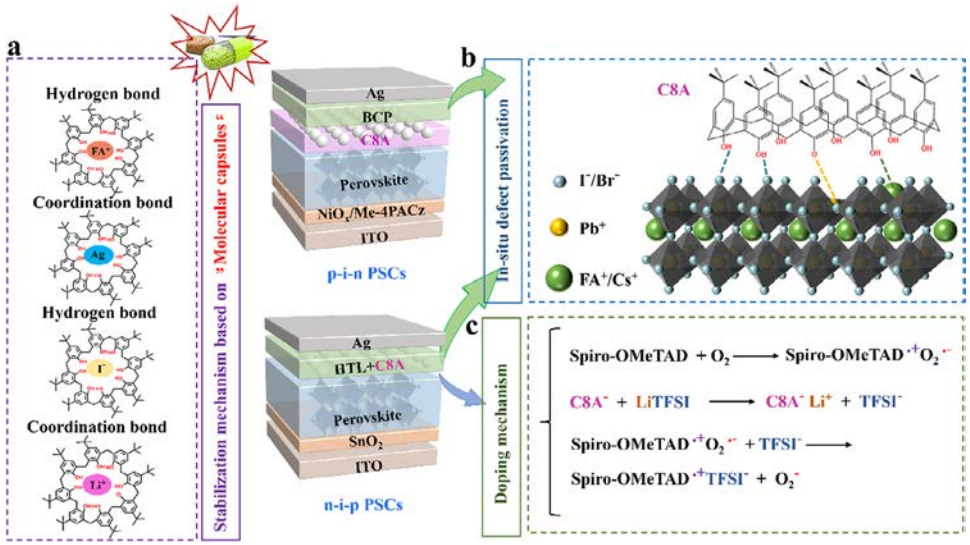

Figure 3. Multifunctionality of C8A. a) Schematic diagram of the immobilization of multiple chemical species by molecular capsule strategy based on host–guest interaction with C8A. b) Schematic diagram of in situ passivation of perovskite surface defects by C8A. c) The mechanisms of accelerated p-doping through C8A.

which is due to reduced nonradiative recombination. To elucidate the relationship between carrier dynamics and C8A doping, the transient photocurrent (TPC) and transient photovoltage (TPV) decay measurements were carried out. From Figure S30 (Supporting Information), after C8A doping, the photocurrent decay lifetime was reduced from 4.99 to 2.48 µs, and the photovoltage decay lifetime was increased from 4.62 to 7.13 µs, indicating that interfacial charge transfer was facilitated and nonradiative combination was suppressed due to improved conductivity of HTL and reduced interfacial defects.

The applicability of our developed ion migration suppression strategy to other perovskite compositions was also checked. To achieve this goal, we fabricated regular planar PSCs based on perovskite films by using a two-step deposition method. As depicted in Figure 4b, a significant increase in PCE from 25.30% (a J_{SC} of 26.20 mA cm^{-2}, a V_{OC} of 1.174 V, and an FF of 82.29%) for the control device to 26.01% (a J_{SC} of 26.47 mA cm^{-2}, a V_{OC} of 1.187 V, and an FF of 82.79%) for the C8A-modified device was realized. This indicates that our molecular capsule strategy based on host–guest interaction with calixarene supramolecules is universal for different perovskite compositions and deposition procedures. One of the most efficient regular PSCs was sent to the National Institute of Metrology (NIM) for certification, achieving a certified PCE of 25.68%, corresponding to a J_{SC} of 26.41 mA cm^{-2}, a V_{OC} of 1.180 V, and an FF of 82.37% (Figure S31, Supporting Information), which is the record PCE ever reported for the TiO_2-based planar PSCs (Figure 4c; Table S1, Supporting Information). Moreover, due to the excellent defect passivation effect of C8A, we used it to modify the upper surface of perovskite films for the fabrication of p-i-n type NiO_x-based inverted PSCs. From Figure 4d and Figure S32 (Supporting Information), the control devices had a PCE of 25.09%, whereas the C8A-modified devices exhibited a PCE of 27.18% (certified 26.79%), which is the highest PCE reported for PSCs fabricated based on vacuum flash evaporation method (Table S2, Supporting Information).

2.7. Long-Term Stability

Finally, we systematically explored the long-term stability of the devices based on Spiro-OMeTAD@Li-TFSI (control) and Spiro-OMeTAD@Li-TFSI-C8A (target) fabricated by a one-step method under different aging conditions according to the International Summit on Organic Photovoltaic Stability (ISOS) protocols.[41] As mentioned previously, the migration of FA^+, I^-, Li^+, and Ag caused by light radiation is the main culprits that accelerate the rapid degradation of the perovskite layer, Ag electrode, and HTL, thereby devastating the longevity of PSCs. For this reason, we tracked the long-term stability of the unencapsulated PSCs at MPP. As illustrated in Figure 4e, the unencapsulated target inverted PSC maintained over 95% of its initial PCE after 1015 h of continuous MPP tracking at 30 ± 5%RH and 25 ± 5 °C, whereas the control device degraded to 67% of its initial PCE. Similarly, Figure 4f illustrates that the control regular device maintained 30% of its original PCE for only 265 h (T_{30}). In stark contrast, the target device with C8A doping showed a T_{80} lifetime of 1015 h. Likewise, the intrinsic stability is also deteriorated due to the migration of FA^+, I^-, Li^+, and Ag facilitated by thermal stress. On account of this, the long-term thermal stability of PSCs was further evaluated under continuous heating at 65 °C in a nitrogen environment (Figure S33, Supporting Information). In a testing period of 1750 h, the PCE of the conventional doping device dropped to 65%. In contrast, the device doped with C8A maintained 91% of its initial PCE under the same aging conditions. Evidently, the thermal stability was dramatically strengthened after C8A doping, which is ascribed to memorably inhibited migration of multiple chemical species. It can be concluded that the light and thermal stabilities could be much heightened by the molecular capsule strategy based on host–guest interaction with calixarene supramolecules. As shown in Figure S34 (Supporting Information), after C8A doping, the hydrophobicity of HTL was markedly increased, which is due to the incorporation of eight hydrophobic tert-butylbenzene rings on C8A molecules.

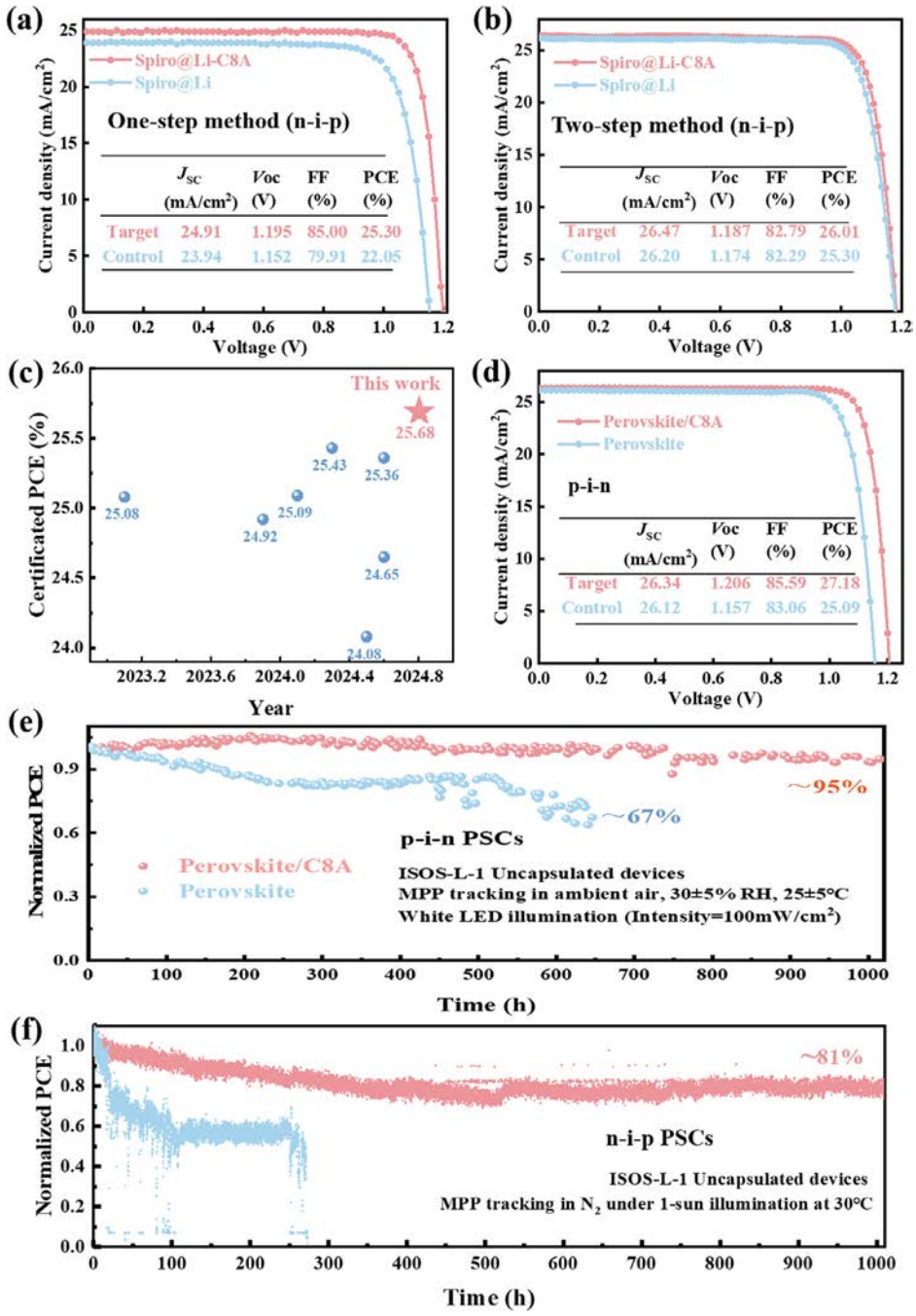

Figure 4. Photovoltaic performance and long-term stability. a) *J--V* curves of the best-performing devices without and with C8A doping based on the perovskite composition $Rb_{0.02}(FA_{0.95}Cs_{0.05})_{0.98}PbI_{2.91}Br_{0.03}Cl_{0.06}$ fabricated by a step method. b) *J--V* curves of the champion devices without and with C8A doping fabricated by two step method. c) Certification PCE comparison between our device and reported high-efficiency regular PSCs. d) *J–V* curves of inverted devices without and with C8A passivation. e) Operational stability of the unencapsulated p-i-n devices without and with C8A modification at MPP under continuous 1 sun irradiation based on ISOS-L-1I protocol. f) Operational stability of the unencapsulated devices without and with C8A doping at MPP under continuous 1 sun irradiation based on ISOS-L-1I protocol.

XRD and UV–vis results confirmed that C8A modification could not only strengthen the moisture resistance of HTL but also protect the underlying perovskite layer from the invasion by ambient moisture (Figures S35 and S36, Supporting Information). Thus, inspired by the excellent ambient humid stability of the C8A-incorporated HTL and perovskite film, we further explored the stability of the devices under a light-shielded environment at 25–35% relative humidity. From Figure S37 (Supporting Information), the C8A-doped device maintained 90% of the initial PCE after 2800 h, while the conventional doped device rapidly

degraded and lost 30% of the initial PCE after 1800 h. Unequivocally, through molecular capsule strategy, the long-term stability was significantly enhanced due to the suppression of multiple mobile chemical species from multiple functional layers, and the photovoltaic performance was much increased due to facilitated p-doping and interfacial defect passivation.

3. Conclusion

In conclusion, we developed a multifunctional universal ion migration suppression strategy that could stabilize the perovskite layer, HTL, and metal electrode layer by simultaneously suppressing the migration of FA^+, I^-, Li^+, and Ag based on host–guest interaction via calixarene supramolecules. Moreover, C8A can facilitate the p-doping of Spiro-OMeTAD and passivate the interfacial defects, which promotes hole extraction and transport as well as suppresses trap-assisted nonradiative recombination. It was proved theoretically and experimentally that among all investigated doping molecules, C8A is optimal in ion migration and defect passivation. The universality of the C8A modulation strategy was revealed by adopting different perovskite films prepared by one-step or two-step deposition methods. As a result, the C8A doped devices based on the one-step deposition method delivered a PCE of 25.30% (certified 24.69%), which is significantly higher than 22.05% of the control device. The C8A doped devices based on the two-step deposition method obtained a PCE of 26.01% (certified 25.68%), which is the highest certificated efficiencies ever reported for TiO_2-based planar PSCs. The C8A modified inverted PSCs attained a peak PCE of 27.18% (certified 26.79%), which is the highest PCE reported for PSCs based on the vacuum flash evaporation technique. Moreover, the C8A-modified unsealed inverted device retained 95% of its initial PCE after 1015 h of continuous operation at MPP tracking. This work provides a feasible and effective avenue to address the intrinsic instability of PSCs by using a creative universal ion migration suppression strategy based on host–guest chemistry with calixarene supramolecules, which paves the way for the commercial application of perovskite photovoltaics and other perovskite-based optoelectronic devices.

Supporting Information

Supporting Information is available from the Wiley Online Library or from the author.

Acknowledgements

This work was financially supported by the National Natural Science Foundation of China (62274018, 52462031), the Xinjiang Construction Corps Key Areas of Science and Technology Research Project (2023AB029), the Tianchi Talent Program of Xinjiang Uygur Autonomous Region (2024, Jiangzhao Chen), and the Key Project of Chongqing Overseas Students Returning to China Entrepreneurship and Innovation Support Plan (cx2023006).

Conflict of Interest

The authors declare no conflict of interest.

Author Contributions

D.H., D.M., J.Z., Y.Y., J.D., and C.L. contributed equally to this work. J.C. and D.H. conceived the idea. J.C. supervised this project. D.H. and D.M. designed the experimental scheme. D.M. fabricated devices and samples for characterization. Y.Y. was responsible for fabricating devices based on the two-step method. J.D. and C.C. fabricated inverted devices and certified the corresponding efficiency. J.C., D.H., and D.M. managed and analyzed data. J.Z. conducted the DFT calculation. Y.Y., X.L., and X.S. assisted in revision and polishing the manuscript language. D.H. wrote the first draft of the manuscript. J.C. and D.H. wrote the final version of the manuscript. All authors discussed the results and contributed to the revisions of the manuscript.

Data Availability Statement

The data that support the findings of this study are available from the corresponding author upon reasonable request.

Keywords

calixareneï¼Œhost–guest interaction, ion migration, perovskite solar cells, stability

Received: March 16, 2025
Revised: May 16, 2025
Published online:

[1] M. J. Paik, Y. Y. Kim, J. Kim, J. Park, S. I. Seok, *Joule* **2024**, *8*, 2073.
[2] J. Zhou, L. Tan, Y. Liu, H. Li, X. Liu, M. Li, S. Wang, Y. Zhang, C. Jiang, R. Hua, W. Tress, S. Meloni, C. Yi, *Joule* **2024**, *8*, 1691.
[3] Y. Gao, Z. Song, Q. Fu, Y. Chen, L. Yang, Z. Hu, Y. Chen, Y. Liu, *Adv. Mater.* **2024**, *36*, 2405921.
[4] Y. Wang, T. Wu, J. Barbaud, W. Kong, D. Cui, H. Chen, X. Yang, L. Han, *Science* **2019**, *365*, 687.
[5] E. Bi, H. Chen, F. Xie, Y. Wu, W. Chen, Y. Su, A. Islam, M. Grätzel, X. Yang, L. Han, *Nat. Commun.* **2017**, *8*, 15330.
[6] C. Ran, J. Xu, W. Gao, C. Huang, S. Dou, *Chem. Soc. Rev.* **2018**, *47*, 4581.
[7] J. Zhang, J. Duan, Q. Guo, Q. Zhang, Y. Zhao, H. Huang, Y. Duan, Q. Tang, *ACS Energy Lett.* **2022**, *7*, 3467.
[8] A. J. Knight, L. M. Herz, *Energy Environ. Sci.* **2020**, *13*, 2024.
[9] H. Back, G. Kim, J. Kim, J. Kong, T. K. Kim, H. Kang, H. Kim, J. Lee, S. Lee, K. Lee, *Energy Environ. Sci.* **2016**, *9*, 1258.
[10] Y. Deng, Q. Dong, C. Bi, Y. Yuan, J. Huang, *Adv. Energy Mater.* **2016**, *6*, 1600372.
[11] A. Guerrero, J. You, C. Aranda, Y. S. Kang, G. Garcia-Belmonte, H. Zhou, J. Bisquert, Y. Yang, *ACS Nano* **2016**, *10*, 218.
[12] S. Du, H. Huang, Z. Lan, P. Cui, L. Li, M. Wang, S. Qu, L. Yan, C. Sun, Y. Yang, X. Wang, M. Li, *Nat. Commun.* **2024**, *15*, 5223.
[13] Y. Zhao, F. Ma, Z. Qu, S. Yu, T. Shen, H.-X. Deng, X. Chu, X. Peng, Y. Yuan, X. Zhang, J. You, *Science* **2022**, *377*, 531.
[14] M. Kim, J. Jeong, H. Lu, T. K. Lee, F. T. Eickemeyer, Y. Liu, I. W. Choi, S. J. Choi, Y. Jo, H.-B. Kim, S.-I. Mo, Y.-K. Kim, H. Lee, N. G. An, S. Cho, W. R. Tress, S. M. Zakeeruddin, A. Hagfeldt, J. Y. Kim, M. Grätzel, D. S. Kim, *Science* **2022**, *375*, 302.
[15] P. Shi, Y. Ding, B. Ding, Q. Xing, T. Kodalle, C. M. Sutter-Fella, I. Yavuz, C. Yao, W. Fan, J. Xu, Y. Tian, D. Gu, K. Zhao, S. Tan, X. Zhang, L. Yao, P. J. Dyson, J. L. Slack, D. Yang, J. Xue, M. K. Nazeeruddin, Y. Yang, R. Wang, *Nature* **2023**, *620*, 323.
[16] D. He, D. Ma, R. Li, B. Liu, Q. Zhou, H. Yang, S. Lu, Z. Zhang, C. Li, X. Li, L. Ding, J. Feng, J. Yi, J. Chen, *ACS Energy Lett.* **2024**, *9*, 2615.

[17] X. Zhang, X. Liu, F. F. Tirani, B. Ding, J. Chen, G. Rahim, M. Han, K. Zhang, Y. Zhou, H. Quan, B. Li, W. Du, K. G. Brooks, S. Dai, Z. Fei, A. M. Asiri, P. J. Dyson, M. K. Nazeeruddin, Y. Ding, *Angew. Chem., Int. Ed.* **2024**, *63*, 202320152.
[18] G. Xie, J. Wang, S. Yin, A. Liang, W. Wang, Z. Chen, C. Feng, J. Yu, X. Liao, Y. Fu, Q. Xue, Y. Min, X. Lu, Y. Chen, *Angew. Chem., Int. Ed.* **2024**, *63*, 202403083.
[19] T. Niu, W. Zhu, Y. Zhang, Q. Xue, X. Jiao, Z. Wang, Y.-M. Xie, P. Li, R. Chen, F. Huang, Y. Li, H.-L. Yip, Y. Cao, *Joule* **2021**, *5*, 249.
[20] J. Yang, X. Pu, T. Wang, S. Cheng, H. Chen, Q. Cao, Y. Zhang, I. Tojiboyev, L. Etgar, F. Ye, *Sol. RRL* **2022**, *6*, 2101101.
[21] G. Qu, L. Dong, Y. Qiao, D. Khan, Q. Chen, P. Xie, X. Yu, X. Liu, Y. Wang, J. Chen, X. Chen, Z.-X. Xu, *Adv. Func. Mater.* **2022**, *32*, 2206585.
[22] B. Liu, X. Ren, R. Li, Y. Chen, D. He, Y. Li, Q. Zhou, D. Ma, X. Han, X. Shai, K. Yang, S. Lu, Z. Zhang, J. Feng, C. Chen, J. Yi, J. Chen, *Adv. Mater.* **2024**, *36*, 2312679.
[23] Y. Shen, K. Deng, Q. Chen, G. Gao, L. Li, *Adv. Mater.* **2022**, *34*, 2200978.
[24] J. Xu, P. Shi, K. Zhao, L. Yao, C. Deger, S. Wang, X. Zhang, S. Zhang, Y. Tian, X. Wang, J. Shen, C. Zhang, I. Yavuz, J. Xue, R. Wang, *ACS Energy Lett.* **2024**, *9*, 1073.
[25] J. Tao, J. Xue, H. Guo, Y. Wang, J. Shen, T. Wang, T. He, G. Fu, S. Yang, *Chem. Eng. J.* **2023**, *463*, 142445.
[26] Q. Dong, M. Chen, Y. Liu, F. T. Eickemeyer, W. Zhao, Z. Dai, Y. Yin, C. Jiang, J. Feng, S. Jin, *Joule* **2021**, *5*, 1587.
[27] B. Liu, Q. Zhou, Y. Li, Y. Chen, D. He, D. Ma, X. Han, R. Li, K. Yang, Y. Yang, S. Lu, X. Ren, Z. Zhang, L. Ding, J. Feng, J. Yi, J. Chen, *Angew. Chem., Int. Ed.* **2024**, *63*, 202317185.
[28] Q. Zhou, B. Liu, Y. Chen, D. Ma, X. Han, D. He, Z. Zhang, H. Yang, P. Zhao, J. Hou, L. Ding, J. Feng, J. Yi, J. Chen, *Nano Energy* **2024**, *124*, 109512.
[29] H. Zhang, F. T. Eickemeyer, Z. Zhou, M. Mladenović, F. Jahanbakhshi, L. Merten, A. Hinderhofer, M. A. Hope, O. Ouellette, A. Mishra, P. Ahlawat, D. Ren, T.-S. Su, A. Krishna, Z. Wang, Z. Dong, J. Guo, S. M. Zakeeruddin, F. Schreiber, A. Hagfeldt, L. Emsley, U. Rothlisberger, J. V. Milić, M. Grätzel, *Nat. Commun.* **2021**, *12*, 3383.
[30] T.-S. Su, F. T. Eickemeyer, M. A. Hope, F. Jahanbakhshi, M. Mladenović, J. Li, Z. Zhou, A. Mishra, J.-H. Yum, D. Ren, A. Krishna, O. Ouellette, T.-C. Wei, H. Zhou, H.-H. Huang, M. D. Mensi, K. Sivula, S. M. Zakeeruddin, J. V. Milić, A. Hagfeldt, U. Rothlisberger, L. Emsley, H. Zhang, M. Grätzel, *J. Am. Chem. Soc.* **2020**, *142*, 19980.
[31] X. Li, H. Yang, A. Liu, C. Lu, H. Yuan, W. Zhang, J. Fang, *Energy Environ. Sci.* **2023**, *16*, 6071.
[32] P. Ferdowsi, S.-J. Kim, T.-D. Nguyen, J.-Y. Seo, J.-H. Yum, K. Sivula, *J. Mater. Chem. A* **2024**, *12*, 15837.
[33] R. Chen, Y. Wu, Y. Wang, R. Xu, R. He, Y. Fan, X. Huang, J. Yin, B. Wu, J. Li, N. Zheng, *Adv. Func. Mater.* **2021**, *31*, 2008760.
[34] X. Wu, Y. Jiang, C. Chen, J. Guo, X. Kong, Y. Feng, S. Wu, X. Gao, X. Lu, Q. Wang, G. Zhou, Y. Chen, J.-M. Liu, K. Kempa, J. Gao, *Adv. Func. Mater.* **2020**, *30*, 1908613.
[35] S. Kennedy, G. Karotsis, C. M. Beavers, S. J. Teat, E. K. Brechin, S. J. Dalgarno, *Angew. Chem., Int. Ed.* **2010**, *25*, 4205.
[36] S. Masi, F. Aiello, A. Listorti, F. Balzano, D. Altamura, C. Giannini, R. Caliandro, G. Uccello-Barretta, A. Rizzo, S. Colella, *Chem. Sci.* **2018**, *9*, 3200.
[37] D. Ma, D. He, Q. Zhu, X. Liu, Y. Yu, X. Shai, Z. Zhang, S. Zhang, J. Feng, J. Yi, *J. Energy Chem.* **2024**, *99*, 277.
[38] Z. Tang, T. Bessho, F. Awai, T. Kinoshita, M. M. Maitani, R. Jono, T. N. Murakami, H. Wang, T. Kubo, S. Uchida, H. Segawa, *Sci. Rep-UK* **2017**, *7*, 12183.
[39] K. Chen, Q. Hu, T. Liu, L. Zhao, D. Luo, J. Wu, Y. Zhang, W. Zhang, F. Liu, T. P. Russell, R. Zhu, Q. Gong, *Adv. Mater.* **2016**, *28*, 10718.
[40] Y. Zheng, R. Su, Z. Xu, D. Luo, H. Dong, B. Jiao, Z. Wu, Q. Gong, R. Zhu, *Sci. Bull.* **2019**, *64*, 1255.
[41] M. V. Khenkin, E. A. Katz, A. Abate, G. Bardizza, J. J. Berry, C. Brabec, F. Brunetti, V. Bulović, Q. Burlingame, A. Di Carlo, *Nat. Energy* **2020**, *5*, 35.